

Onset of Driven Collisionless Reconnection in Strongly Magnetized Pair Plasmas

CAMILLE GRANIER ¹, DANIEL GROŠELJ ¹, LUCA COMISSO ^{2,3} AND FABIO BACCHINI ^{1,4}

¹*Centre for mathematical Plasma Astrophysics, Department of Mathematics, KU Leuven,
Celestijnenlaan 200B, B-3001 Leuven, Belgium*

²*Department of Physics, Columbia University, New York, NY 10027, USA*

³*Department of Astronomy, Columbia University, New York, NY 10027, USA*

⁴*Royal Belgian Institute for Space Aeronomy, Solar-Terrestrial Centre of Excellence,
Ringlaan 3, 1180 Uccle, Belgium*

ABSTRACT

We investigate the onset of driven collisionless reconnection and plasmoid formation in a magnetically dominated pair plasma, using 2D particle-in-cell simulations. Two force-free flux tubes of radius R are initially pushed together with a prescribed velocity, forming a current sheet whose width shrinks until reconnection sets in. Even in our largest simulation with $R \approx 1600$ plasma skin depths, the sheet thickness at reconnection onset is comparable to the skin depth. Plasmoid chains are seen to develop when the sheet aspect ratio $A \gtrsim 30$. In the strongly magnetized limit, the onset of reconnection occurs in roughly 2 to 6 light-crossing times R/c , depending on the imposed driving timescale, which controls the duration of the linear tearing phase. In the subsequent nonlinear merging phase, the evolution becomes effectively independent of the initially imposed velocity, leading to magnetic energy dissipation consistent with a normalized reconnection rate ~ 0.1 . Our results have important implications for explosive release of magnetic energy in magnetospheres of compact objects and their surroundings.

Keywords: High energy astrophysics (739); Plasma physics (2089); Magnetic fields (994); Non-thermal radiation sources (1119); Particle astrophysics (96)

1. INTRODUCTION

Magnetic reconnection is ubiquitous astrophysical plasmas. It is believed to power the explosive release of magnetic energy in solar flares (E. N. Parker 1957). By analogy with solar flares, reconnection-powered emission mechanisms have been applied to more distant high-energy signals, such as flares from pulsar wind nebulae (D. A. Uzdensky et al. 2011; B. Cerutti et al. 2013), and high-energy outbursts from neutron-star and black-hole magnetospheres (C. Thompson 1994; M. Lyutikov et al. 2003). Reconnection in these high-energy environments takes place in the relativistic regime (L. Sironi et al. 2025). Kinetic particle simulations have shown that reconnection in relativistic astrophysical plasmas can indeed accelerate particles efficiently (e.g., L. Sironi & A. Spitkovsky 2014; F. Guo et al. 2014; G. R. Werner et al. 2016) and power high-energy emission (B. Cerutti et al. 2013; H. Zhang et al. 2020; H. Hakobyan et al. 2023b; A. Chernoglazov et al. 2023; L. Comisso & B. Jiang 2023; J. Mehlhaff et al. 2024), yet much about the physics of relativistic reconnection remains to be understood.

Magnetic reconnection is facilitated by non-ideal electric fields, which develop most notably near electric current sheets. Resistive magnetohydrodynamic (MHD) studies revealed key aspects of the onset of reconnection

in evolving current sheets (e.g., D. Biskamp 1986; K. Shibata & S. Tanuma 2001; N. F. Loureiro et al. 2007; D. A. Uzdensky & N. F. Loureiro 2016; L. Comisso et al. 2016; Y.-M. Huang et al. 2017), but many astrophysical plasmas are effectively collision-free. Reduced fluid models incorporating Hall effects and electron-MHD physics capture some kinetic behavior (D. Del Sarto et al. 2016; F. Pucci et al. 2017; C. Shi et al. 2019; A. Mallet 2020), yet a detailed fully kinetic investigation of how sheets form and eventually reconnect is presently lacking.

Moreover, most kinetic and fluid simulations begin from an already formed current sheet which reconnects spontaneously. This involves setups featuring Harris sheets (T. J. Schep et al. 1994; F. Porcelli 1991), coalescing islands (D. A. Uzdensky & R. M. Kulsrud 2000; A. Bhattacharjee et al. 2009; Y.-M. Huang & A. Bhattacharjee 2010), or repelling force-free channels (R. Keppens et al. 2014; B. Ripperda et al. 2017a,b), to name a few. However, current sheets often form and reconnect under the action of external forces. Examples include the Taylor problem (T. S. Hahm & R. M. Kulsrud 1985; J. Birn et al. 2005; L. Comisso et al. 2015) or merging flux tubes pushed together by converging flows (M. Lyutikov et al. 2017; B. Ripperda et al. 2019).

Near compact objects, magnetic structures can coalesce explosively when twisted and sheared by strong flows and relativistic frame-dragging effects. Relevant examples include twisted magnetar magnetospheres (K. Parfrey et al. 2013), colliding flux tubes in pulsar magnetospheres (J. F. Mahlmann et al. 2023), frame-dragging–twisted tubes between a black-hole ergosphere and disk (S. Koide et al. 2006), and loops in a turbulent accretion-disk corona (D. A. Uzdensky & J. Goodman 2008; F. Yuan et al. 2009). In these magnetically dominated plasmas the Alfvén speed approaches the speed of light c , which enables rapid variability on the light-crossing time scale. Thus, the problem of collisionless reconnection onset in the strongly magnetized regime is of prime interest for understanding the observed time scales of electromagnetic flares in relativistic astrophysical plasmas (e.g., H. Krawczynski et al. 2004; A. A. Abdo et al. 2011; Y. Yuan et al. 2016; B. Ripperda et al. 2022; GRAVITY Collaboration et al. 2021). Here, we aim to fill a gap in the literature by studying the dynamics of current sheets in collisionless pair plasmas over their full lifetime, from formation to the final stages of the reconnection process, using 2D particle-in-cell (PIC) simulations.

Global PIC simulations can self-consistently describe the formation of current sheets in realistic geometries, but they remain far from achieving real astrophysical scale separations. For example, in the presently largest 3D simulations of pulsar magnetospheres, the light-cylinder radius is only about 200 times larger than the plasma skin depth (H. Hakobyan et al. 2023a). Similarly, in global PIC simulations of black-hole magnetospheres, the gravitational radius typically measures only about 20 plasma skin depths in size (K. Parfrey et al. 2019; B. Crinquand et al. 2022; I. El Mellah et al. 2023; A. Galishnikova et al. 2023). Therefore, in order to achieve a maximum possible scale separation and to study the onset problem under well controlled initial conditions, we focus here on local PIC simulations, featuring two isolated and initially force-free magnetic flux tubes.

2. METHODOLOGY

All of our simulations are carried out with the PIC code TRISTAN-MP v2 (H. Hakobyan et al. 2023c). We perform 2D simulations using an electron–positron pair plasma. We use the configuration inspired by Lundquist’s force-free cylinders (M. Lyutikov et al. 2017; B. Ripperda et al. 2019). Inside each flux tube of radius R , the poloidal magnetic field is given by

$$B_\phi(r) = B_0 \mathcal{J}_1(\alpha r/R) \quad (1)$$

and the vertical (i.e., out-of-plane) magnetic field by

$$B_z(r) = B_0 \sqrt{\mathcal{J}_0(\alpha r/R)^2 + C}, \quad (2)$$

where r is the distance from the center of the tube, \mathcal{J}_0 and \mathcal{J}_1 are Bessel functions of the first kind, $\alpha = 3.8317$ (the first zero of \mathcal{J}_1), $C = 0.01$, and B_0

is a reference magnetic field strength. The solutions (1) and (2) are truncated at $r = R$. Outside the two flux tubes, the in-plane magnetic field is zero and $B_z = B_0 \sqrt{\mathcal{J}_0(\alpha)^2 + C}$. The flux tubes carry no net current at the start of the simulation, so that they do not attract each other. We employ a square simulation domain of size $L_x = L_y = 4R$. The two flux tubes are initially located at $\mathbf{r}_1 = (x_1, y_1) = (2R, R)$ and $\mathbf{r}_2 = (x_2, y_2) = (2R, 3R)$. To initiate the current sheet formation, we push the tubes toward each other with a prescribed initial velocity v_{push} , corresponding to a driving timescale $t_{\text{drive}} = R/v_{\text{push}}$. The initial electric field inside each flux tube is given by $\mathbf{E} = -\mathbf{v}_{\text{push}} \times \mathbf{B}/c$. Our simulation box is initially filled with a cold pair plasma with uniform density n_0 and temperature $T_0 = 0.005 m_e c^2$. The electron and positron distributions inside each tube are initialized with bulk motion profiles consistent with Ampère’s law and the $\mathbf{E} \times \mathbf{B}$ drift motion. We perform simulations for a range of different plasma magnetizations $\sigma_0 = B_0^2/4\pi n_0 m_e c^2$, box sizes, and initial push velocities. The magnetization σ_0 based on the reference field strength B_0 ranges from 25 to 800. We note that the *average in-plane* magnetization *inside* the tubes $\sigma_{\text{in}} \approx 0.16\sigma_0$. We explore a range of computational domain sizes, from $L_x = 204.8 d_{e0}$ to $L_x = 6553.6 d_{e0}$, where $d_{e0} = c/\omega_p$ is the cold plasma skin depth, and $\omega_p = \sqrt{4\pi n_0 q^2/m_e}$ is the plasma frequency. Thus, the flux tube radius R ranges from roughly $38 d_{e0}$ to $1638 d_{e0}$ in our set of runs. Our numerical resolution is $\Delta x = d_{e0}/5$, where Δx is the grid cell size.⁵ We use 256 particles per cell.⁶ For reference, we show spatial profiles of the initial magnetic field configuration in Appendix A. This shows that the guide field (B_z) exhibits a nontrivial profile, which is needed to impose the force-free property of the initial condition. The guide field peaks at the centers of the tubes, decreases toward the edges, and exhibits a slight bump near the region of contact between the tubes.

3. RESULTS

3.1. Description of the Evolution

We identify three distinct phases in the evolution of the system (see Fig. 1):

- *Phase I (Sheet Formation)*: The flux tubes are externally driven to approach each other, resulting in the formation of a thin current sheet (Fig. 1(a)). A single X-point develops, while small-scale perturbations in the form of tearing modes (see e.g. H. P. Furth et al. 1963; B. Coppi et al. 1976; L. M. Zelenyi & V. V. Krasnoselskikh 1979) grow linearly (Fig. 1(f)).

⁵ Simulations using $\Delta x = d_{e0}/10$, and a correspondingly larger number of cells to maintain the same R/d_{e0} yielded results identical to those with 5 cells per skin depth.

⁶ Convergence tests were performed with 96, 128, and 256 particles per cell.

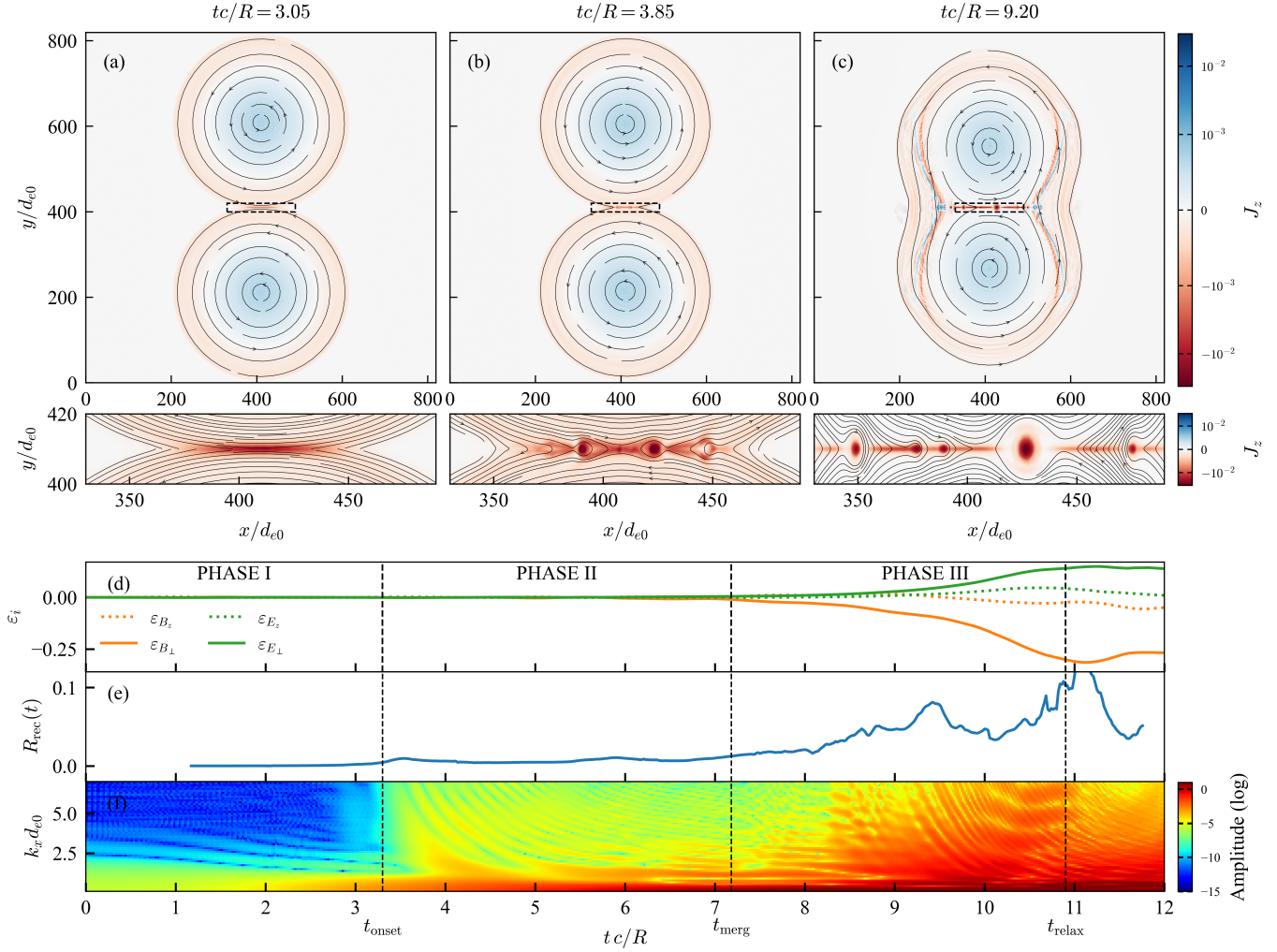


Figure 1. (a)–(c): Contours of out-of-plane current density J_z (color scale) and magnetic field lines (black) during the evolution of the flux tubes. The dashed black boxes mark the regions shown in the zoomed-in view below. (d): Temporal evolution of the energy components, $\varepsilon_i = E_i(t) - E_i(0)/E_{B_\perp}(0)$. (e): Time evolution of the normalized reconnection rate. (f): k_x -spectra of the magnetic flux function averaged inside the current sheet (over $10d_{e0}$ along y). The color-coded intensity represents the logarithmic amplitude of the wavenumbers. Key time thresholds (t_{onset} , t_{merg} and t_{relax}) are indicated by vertical dashed lines. This simulation was run with $v_{\text{push}} = 0.05c$ ($t_{\text{drive}} = 20R/c$), $\sigma_0 = 50$ ($\sigma_{\text{in}} = 8$), and $R/d_{e0} = 205$.

- *Phase II (Plasmoid Formation)*: When the tearing-mode driven fluctuations grow to sufficient amplitude to halt the thinning process, the instability transitions to the nonlinear regime. Nonlinear mode coupling can be observed as a yellow “zebra” pattern in panel (f). We denote the onset of this transition by the time t_{onset} , which we identify as the time at which the sheet reaches minimum thickness. The sheet then fragments into multiple plasmoids (panel (b)), leading to an increase in the reconnection rate (panel (e)).
- *Phase III (Merging)*: In the final phase, the flux tubes coalesce rapidly, causing a fast conversion of magnetic energy (panel (d)). We denote the beginning of the merging process by t_{merg} (i.e.,

when the conversion of in-plane magnetic energy reaches 1%), and the time when the flux tubes relax toward a quasi-stable configuration by t_{relax} (i.e., when the conversion reaches 30%). The duration of the merging phase is given by $\Delta t_{\text{merg}} = t_{\text{relax}} - t_{\text{merg}}$.

3.2. Current Sheet Formation and Collapse

We first examine the formation of the current sheet. The sheet thickness $a(t)$, measured in units of d_{e0} , is determined by applying a polynomial fit to the transverse profile of the out-of-plane current density J_z (e.g., see also Y.-M. Huang et al. 2017). The sheet boundaries are at the positions where J_z reaches two-thirds of its maximum value. Fig. 2 shows the evolution in time of

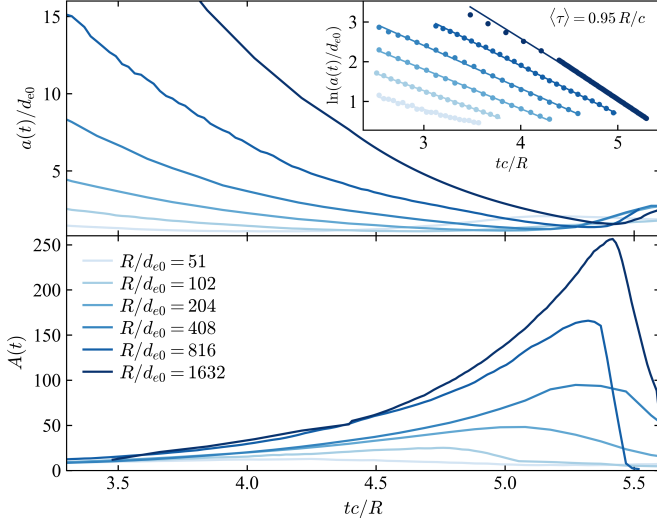


Figure 2. Time evolution of the normalized current sheet width, $a(t)/d_{e0}$, and the aspect ratio, $A(t) = \ell(t)/a(t)$, for different system sizes at $\sigma_{in} = 8$. Inset: the evolution of $\ln(a(t)/d_{e0})$, showing the exponential thinning.

the sheet width and aspect ratio, $A(t) = \ell(t)/a(t)$, where ℓ is the current sheet length, for several R/d_{e0} .

During Phase I, the external push induces a kinematic linear thinning of the sheet due to the frozen-in condition: $a(t) \simeq R - v_{push} t$, until self-pinching effects by the magnetic force become non-negligible. Then, the collapse accelerates, transitioning from a linear to an exponential thinning regime. In the inset of Fig. 2 we show $\ln(a(t)/d_{e0})$ during the accelerated stage of the collapse, confirming that the thinning is of the form $a(t - t_K) \simeq a_K \exp(-(t - t_K)/\tau)$, where τ is the exponential thinning time scale, a_K is the initial width, and t_K is the time when exponential collapse begins. An analytical estimate, which we provide in Appendix B, gives a value of the prefactor $a_K = a(0) \simeq Rv_A/(v_A + v_{push})$, and $\tau \simeq R/(v_A + v_{push})$, where v_A is the Alfvén speed based on the in-plane field upstream of the sheet. Both the initial sheet width a_K and the exponential thinning time scale τ are roughly proportional to R . As seen in Fig. 2, the rate of exponential collapse in units of R/c is slightly faster in larger-size systems. We note that we mainly focus on the regime where $v_{push} < v_A$. In this case, the magnetic pinch force keeps the forming current sheet from breaking apart. In the opposite limit ($v_{push} \gtrsim v_A$), the sheet thinning proceeds in the linear (kinematic) regime, but without any restoring force to hold the sheet together. In our simulations, this leads to sharp wave-like disturbances in the current density (not shown here), which propagate away from the sheet toward the flux-tube cores.

The current sheet thinning coincides with the linear growth of tearing modes. When the tearing modes grow sufficiently in amplitude to become nonlinear, the thin-

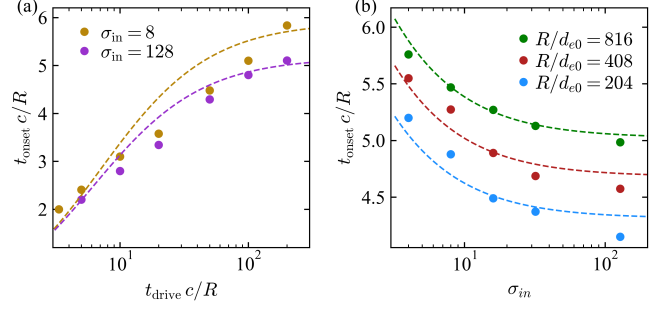


Figure 3. (a): Reconnection onset times as a function of the driving timescale for $\sigma_{in} = 8$ and $\sigma_{in} = 128$ at $R/d_{e0} = 204$. (b): Onset times as a function of in-plane magnetization for $t_{drive}c/R = 50$. The dashed lines show the theoretical estimate (3).

ning stops and reconnection sets in. Thus, we define the onset time as the time when the sheet thickness reaches its minimum. In Appendix B we derive an estimate for the onset time of the form

$$t_{onset} \simeq \frac{R}{v_A + v_{push}} \left[1 + \ln \frac{a_K}{d_{e0}} \right], \quad (3)$$

where the first term is the duration of the kinematic linear thinning phase and the second term is the duration of the exponential collapse phase. Fig. 3(a) shows that t_{onset} increases with the driving timescale $t_{drive} = R/v_{push}$, in good agreement with Eq. (3). Panel (b) shows that t_{onset} depends only weakly on the exact value of the magnetization when $\sigma_{in} \gtrsim 1$; varying σ_{in} by more than an order of magnitude changes t_{onset} by only tens of percent. This arises because the magnetization enters t_{onset} in Eq. (3) only via the Alfvén speed, which is always close to c for our set of runs. We also find that the normalized collapse time, $t_{onset} c/R$, grows only logarithmically with the system size R/d_{e0} , which is consistent with the second term in Eq. (3).

For system sizes from $R/d_{e0} \approx 50$ to ≈ 1600 , we find that the sheet thickness $a(t_{onset}) = a_*$ at reconnection onset depends very weakly on the system size; it scales roughly as $a_* \sim d_{e0}(R/d_{e0})^{0.08}$ (see also Fig. 2). We note that our numerical experiments are outside the formal range of validity of existing onset theories, where the thickness at disruption a_* is assumed much greater than the inner layer width $\sim d_{e0}$ (e.g., N. F. Loureiro & S. Boldyrev 2018; L. Comisso & L. Sironi 2019). Our simulations show that the dependence of a_* on σ_{in} is also minimal. Moreover, when varying the drive velocity from $v_{push} = 0.02c$ to $0.2c$, the measured collapse width changes only from $1.10d_{e0}$ to $1.16d_{e0}$, demonstrating that a_* is also essentially independent of the push magnitude.

We also measure the length ℓ of the evolving current sheet. The length at collapse ℓ_* increases with the system size roughly as $\ell_* \sim 0.3(R/d_{e0})^{1.08}$. Therefore, the critical sheet aspect ratio $A_* = \ell_*/a_*$ scales

roughly as $A_* \sim 0.3R/d_{e0}$. Based on earlier works (e.g., W. Daughton et al. 2011; H. Ji & W. Daughton 2011), a current sheet should break into plasmoids when its length exceeds roughly 100 times its width. In our numerical experiments, this threshold appears to be roughly at $A_* \gtrsim 30$. For the cases shown in Fig. 2 with $v_{\text{push}} = 0.02c$, the simulation with $R/d_{e0} = 51$ does not form plasmoids, but plasmoids appear in simulations with larger boxes. As we discuss in the next section, the push velocity influences the number of plasmoids formed, since it affects the amplitude of perturbations and to some extent also the geometry of the current sheet. For the system size $R/d_{e0} = 204$, at the lowest background speed, $v_{\text{push}} = 0.005c$, the current sheet length at disruption is approximately $\ell_* \approx 40d_{e0}$, while at the highest speed, $v_{\text{push}} = 0.2c$, we find $\ell_* \approx 96d_{e0}$.

Therefore, shorter driving time scales, corresponding to higher background flow speeds, result in somewhat larger sheet aspect ratios.

3.3. Plasmoids

In the bottom panel of Fig. 1, the k_x -spectrum of the magnetic flux function, averaged over $10d_{e0}$ across the current sheet, is shown. We observe that during Phase I the modes satisfying $k_x d_{e0} \lesssim 1$ exhibit a linear growth. In Fig. 8 of Appendix C we show how the growth rates of modes with different k_x evolve with time in one of our simulations, confirming that the disruption is preceded by a phase with linear growth. At time t_{onset} , the non-linear Phase II begins with numerous unstable modes, leading to the formation of plasmoids (see Fig. 4(a) at $tc/R = 5.86$). These plasmoids are then expelled from the current sheet by the outflow faster than they can grow. Once expelled, the current aligns along the separatrices, producing a characteristic open outflow structure ($tc/R = 7.42$ – 12.89). When fast merging starts, the current sheet stretches and thins again, reaching a minimum thickness of approximately $0.6d_{e0}$. This brings higher- k_x modes into the nonlinear regime, leading to a new generation of plasmoids ($tc/R = 15.23$). Overall, plasmoid formation is closely linked to whether we see modes with $k_x d_{e0} \gtrsim 1$ reaching large amplitudes during Phase II and III.

In Fig. 4(b), the red curve shows the maximum number of plasmoids observed simultaneously during Phase II, while the blue curve shows their spacing, estimated from the separation between magnetic O-points. The circles denote slow driving ($t_{\text{drive}} = 50R/c$) and the stars denote fast driving ($t_{\text{drive}} = 2.5R/c$). For $R/d_{e0} = 204$, fast driving yields four times as many plasmoids with a shorter plasmoid separation of about $l_{pl} \approx 7d_{e0}$, suggesting that a stronger external push leads to a denser plasmoid chain. We observe that the number of plasmoids during Phase II scales as $N \propto R/d_{e0} \propto A$. The effective aspect ratio of the inter-plasmoid current sheets is roughly $A \lesssim 10$, in agreement with previous studies (e.g., C. Granier et al. 2022; M. Petropoulou et al. 2018).

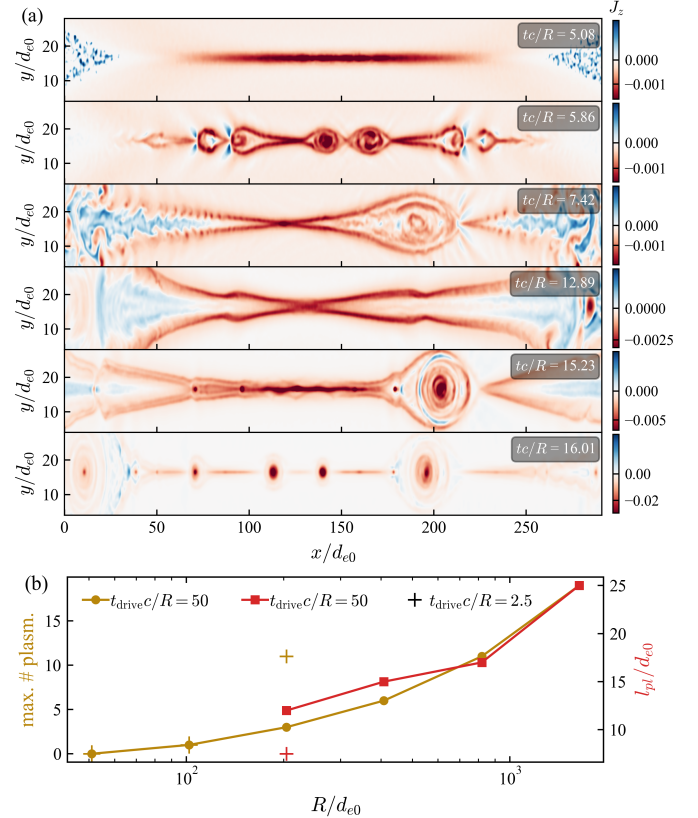


Figure 4. (a): Evolution of the current density J_z for $R/d_{e0} = 408$ and $v_{\text{push}} = 0.02c$. (b): Maximum number of plasmoids and the minimum inter-plasmoid distance at the start of Phase II as functions of the system size R/d_{e0} , for $t_{\text{drive}} = 50R/c$ ($v_{\text{push}} = 0.02c$) and $\sigma_{\text{in}} = 8$. The stars are showing the same quantities for a shorter driving time, $t_{\text{drive}} = 2.5R/c$ ($v_{\text{push}} = 0.4c$).

3.4. Reconnection Rate

The normalized reconnection rate is measured as

$$R_{\text{rec}}(t) = \frac{1}{v_A B_{x\text{up}}} \frac{d}{dt} \left[\max(A_z) - \min(A_z) \right], \quad (4)$$

where A_z is the out-of-plane component of magnetic vector potential in the midplane between the two tubes (i.e., along the current sheet), and $B_{x\text{up}}$ and v_A are the upstream reconnecting field and Alfvén speed (based on $B_{x\text{up}}$). Eq. (4) measures how fast the magnetic flux is being transferred across the separatrix. The time-averaged value of R_{rec} during Phase II for different push velocities at $R/d_{e0} = 204$ is shown on panel (a) of Fig. 5. We find that the reconnection rate during Phase II is strongly sensitive to the push velocity v_{push} , while its dependence on the magnetization and system size is weak. As σ_{in} increases from 8 to 128, the rate decreases slightly from ~ 0.036 to ~ 0.020 . Increasing R by a factor of 2 yields a minor drop from ~ 0.024 to ~ 0.020 . Panel (b) of Fig. 5 shows the time evolution of the reconnection rate

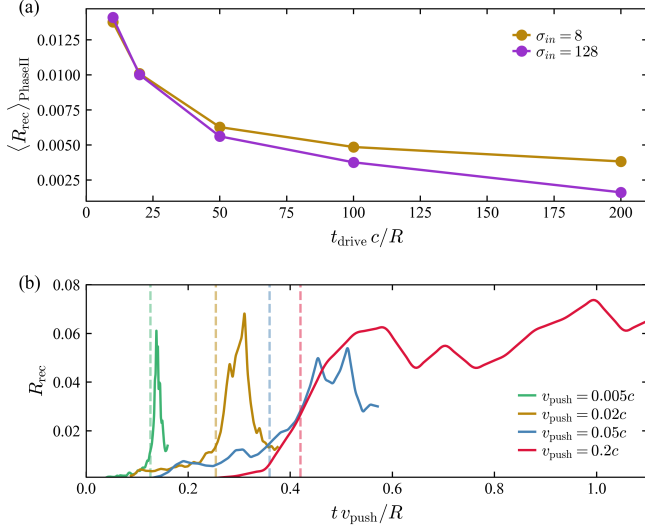


Figure 5. Reconnection rate R_{rec} as measured via Eq. (4). (a): values time-averaged over Phase II (i.e., from t_{onset} to t_{merg} , where t_{merg} marks the beginning of the merger Phase III). (b): evolution of R_{rec} in time for various v_{push} . Dashed vertical lines mark t_{merg} .

for different push velocities. The measured reconnection rates are somewhat below the typical ~ 0.1 value (with v_A based on the in-plane field), which is consistent with the presence of a moderate guide field in our numerical experiments (e.g., see L. Sironi et al. 2025, as well as Appendix A for the initial guide-field profile).

3.5. Fast Merging

All simulations, regardless of magnetization, system size, or push, converge to a similar reconnection rate during the final fast merging phase. The typical value of the rate is close to, but somewhat below 0.1, even for strong driving with $v_{\text{push}} > 0.1c$. The near-universal reconnection rate during Phase III implies that the available magnetic energy (inside the tubes) is dissipated at a rate that is largely independent of the initial condition. To capture the net rate at which the in-plane magnetic energy is dissipated during the merging, we define

$$\mathcal{R}_{\text{diss}} = \frac{R}{cE_{B\perp}(0)} \frac{d(-E_{B\perp}(t))}{dt} \quad (5)$$

which provides an alternative estimate for the effective reconnection rate, based on the net loss of reconnecting magnetic energy. While Eq. (4) measures the instantaneous reconnection rate at the main X-point, $\mathcal{R}_{\text{diss}} \simeq 2R_{\text{rec}}$ measures the energy-conversion efficiency over the merging process.⁷ As shown in Fig. 6, the duration of the merger phase Δt_{merg} is roughly $2R/c$, during

⁷ The factor 2 comes from the Poynting flux bringing reconnecting magnetic energy from both sides of the current sheet at about the same rate.

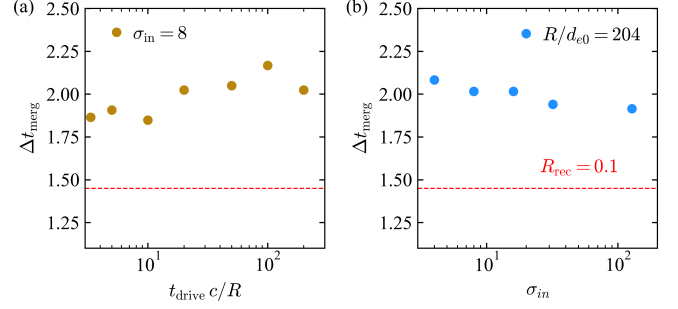


Figure 6. (a): Normalized merging duration Δt_{merg} in units of R/c as a function of the driving timescale for $\sigma_{\text{in}} = 8$ and $R/d_{e0} = 204$. (b): Δt_{merg} as a function of in-plane magnetization for $t_{\text{drive}} c/R = 50$. The start of the merger phase is defined as the time at which 1% of the initial magnetic energy has been dissipated. The end of the merger phase is determined as the time at which the amount of dissipated energy saturates at about 30% (see Fig. 1).

which about 30% of the initial magnetic energy is dissipated (see Fig. 1). Thus, the energy is dissipated at an average rate of $\langle R_{\text{diss}} \rangle \approx 0.15$.

4. DISCUSSION AND CONCLUSION

We investigated the onset of driven collisionless reconnection in a strongly magnetized pair plasma. Our 2D PIC simulations feature two force-free flux tubes of radius R , which are initially pushed together with a prescribed velocity v_{push} to trigger current sheet formation. We study the full lifespan of the evolving system, from current sheet formation, to reconnection onset, and finally into the nonlinear flux-tube merger phase. At high magnetizations ($\sigma_{\text{in}} \gg 1$), the reconnection onset time t_{onset} is of the order of the light-crossing time R/c . In units of the light-crossing time, t_{onset} depends weakly on the flux tube radius and on the magnetization, but changes with the imposed driving timescale $t_{\text{drive}} = R/v_{\text{push}}$ as $t_{\text{onset}} \sim R/(v_A + v_{\text{push}})$. This indicates that the external driving significantly influences the duration of the current-sheet formation, as well as the duration of the linear tearing phase. In realistic astrophysical environments, the driving timescale may be determined by various processes. In magnetospheres of compact objects and their surroundings this involves most notably formation of current sheets via shearing and twisting of magnetic field lines, induced by the rapid rotation of the central object (K. Parfrey et al. 2013; K. Parfrey et al. 2014; Y. Yuan et al. 2019; J. F. Mählmann et al. 2020; B. Ripperda et al. 2020, 2022; I. El Mellah et al. 2023).

Even in our largest simulations with $R/d_{e0} \approx 1600$, we find that the forming current sheet thins exponentially until its thickness a reaches the skin-depth scale: $a_* \sim d_{e0}$. The aspect ratio at the moment of disruption scales as $A_* = \ell_*/a_* \sim 0.3R/d_{e0}$. When $A_* \gtrsim 30$ plasmoids appear, and below this threshold only a single

X-point forms. This implies that the smallest reconnecting current sheet that becomes plasmoid-unstable in our simulations has a length of at least $30 d_{e0}$. For asymptotically large domains, we expect that disruption occurs when the sheet thickness $a_* \gg d_{e0}$, as anticipated theoretically (e.g., L. Comisso & L. Sironi 2019). Our results thus indicate that the asymptotic regime in a magnetically dominated pair plasma requires $R \gg 10^3 d_{e0}$; the exact size for the presumed transition into the asymptotic regime is presently unknown (i.e., our results only provide a lower bound). Further work is needed to clarify how our results extrapolate to much larger domains.

We measure reconnection rates which are largely insensitive to system size and magnetization, but scale with the driving velocity during the initial (pre-merger) stage of reconnection. In the highly nonlinear phase, once fast merging has started, the reconnection rate becomes effectively independent of the initially imposed driving timescale, and proceeds at a normalized rate close to ~ 0.1 , in accordance with theoretical and simulation results on standard collisionless reconnection in preexisting current sheets (L. Comisso & A. Bhattacharjee 2016; M. Goodbred & Y.-H. Liu 2022).

Our results constrain the timescales of reconnection-driven flares in high-energy astrophysical environments, such as pulsar wind nebulae (A. A. Abdo et al. 2011), black-hole accretion flows (GRAVITY Collaboration et al. 2021), blazar jets (H. Krawczynski et al. 2004), or magnetospheres of magnetars (S. Mereghetti et al. 2024). Essentially, we find that reconnection of magnetically dominated flux tubes typically develops on a timescale of a few light-crossing times. After the onset, the sheet

fragments into a chain of plasmoids. The first plasmoids are expelled from the sheet by the reconnection outflows. We expect a weak emission during the early stage of reconnection, which typically lasts a few R/c . This is followed by a more violent flux-tube merger phase, featuring a new generation of plasmoids, which corresponds to the peak of the dissipation and is largely insensitive to the details of the driving mechanism. Future work will investigate particle acceleration and the emerging electromagnetic emission during all stages of the reconnection process.

ACKNOWLEDGMENTS

C.G. thanks L. Sironi, and I. Demidov for helpful discussions. D.G. also thanks L. Sironi for sharing his unpublished results on flux-tube mergers. F.B. acknowledges support from the FED-tWIN programme (profile Prf-2020-004, project “ENERGY”), issued by BELSPO, and from the FWO Junior Research Project G020224N granted by the Research Foundation – Flanders (FWO). D.G. is supported by the FWO Senior Postdoctoral Fellowship 12B1424N. L.C. acknowledges support from the NASA ATP award 80NSSC22K0667 and the National Science Foundation award PHY-2308944. The resources and services used in this work were provided by the VSC (Flemish Supercomputer Center), funded by the FWO and the Flemish Government.

Software: TRISTAN-MP v2 (H. Hakobyan et al. 2023c)

APPENDIX

A. INITIAL MAGNETIC FIELD PROFILES

In Fig. 7 we show the initial 1D magnetic field profiles of B_x and B_z along the y direction at $x = 2R$, with $R/d_{e0} = 204$. The two flux tubes are centered at $\mathbf{r}_1 = (x_1, y_1) = (2R, R)$ and $\mathbf{r}_2 = (x_2, y_2) = (2R, 3R)$. The point of contact, where the current sheet eventually forms, is located at $y = 2R$. The poloidal component B_x vanishes at the center of the domain. The guide field B_z exhibits a nontrivial profile around the region where the sheet forms.

B. DRIVEN CURRENT SHEET THINNING

To gain insight into the driven current-sheet formation, we adopt a 1D symmetric current-sheet approximation in a collisionless, cold plasma at scales above particle inertia and other nonideal effects, so that the magnetic field is frozen-in. Given that our main focus is the magnetically dominated regime, we neglect the kinetic pressure in the following analysis. We assume that the reconnecting field reverses linearly inside a sheet of half-width $a(t)$,

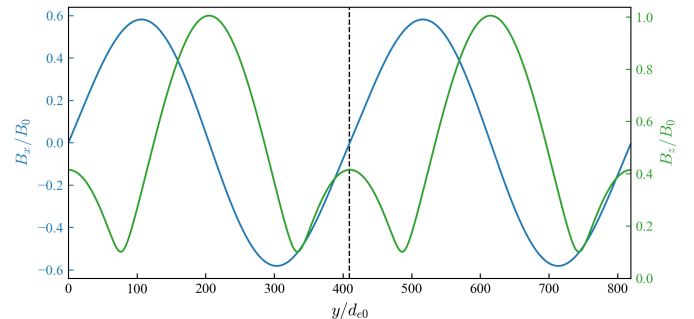


Figure 7. Initial 1D profiles of the initial magnetic field components $B_x(x=2R, y)$ and $B_z(x=2R, y)$ for a flux tube radius of $R/d_{e0} = 204$. The dashed vertical line indicates the position where the current sheet forms.

such that $B_{xup} y/a(t)$, for $|y| \leq a(t)$, and $\pm B_{xup}$, for $|y| > a(t)$.

Kinematic Thinning.—In this initial phase, the sheet half-width a remains large ($a \approx R$), so that self-pinch

forces $\sim v_A^2/a$ are negligible compared to the imposed inflow. The imposed inflow, $v_y(\pm a) = \mp v_{\text{push}}$, drives the sheet edges inward at constant speed. Hence,

$$a(t) = R - v_{\text{push}} t, \quad 0 \leq t \leq t_K, \quad (\text{B1})$$

where the key assumption $R \gg a_K$ allows us to neglect pinch acceleration until $t = t_K$. The transition time t_K is defined as the moment when the Lorentz-pinch acceleration becomes comparable to the driving compression, and the sheet half-width at that moment is $a_K \simeq R - v_{\text{push}} t_K$.

Self-Consistent (Exponential) Collapse.—For $t \geq t_K$, the sheet has been sufficiently compressed so that the drift current $J_z \sim B_{x\text{up}}/(4\pi a_K)$ generates a Lorentz-pinch force $(\mathbf{J} \times \mathbf{B})_y = J_z B_{x\text{up}} = \rho v_y \partial_y v_y$ dominating the external push, causing self-collapse. Since the guide field within the current sheet remains very weak and is continually advected out of the layer by the outflow, the term $J_x B_z$ is negligible compared to the $J_x B_{x\text{up}}$ pinch force. This yields the self-similar inflow profile

$$v_y(y) \simeq -y/\tau \quad \text{with} \quad \tau = \frac{a_K}{v_A}, \quad v_A = \frac{B_{x\text{up}}}{\sqrt{4\pi\rho}}. \quad (\text{B2})$$

Hence, the sheet edge obeys $da/dt = v_y(a(t)) = -a(t)/\tau$, which gives

$$a(t - t_K) = a_K \exp[-(t - t_K)/\tau]. \quad (\text{B3})$$

Matching the Phases—To determine quantitatively when the kinematic thinning gives way to the exponential collapse, we compare the time it takes the external drive to compress the sheet from its initial half-width R down to a_K , namely $t_{\text{push}} \simeq (R - a_K)/v_{\text{push}}$, with the Alfvén-crossing time across the compressed half-width, $t_A \simeq a_K/v_A$. At the transition these two timescales are equal. This gives

$$a_K \simeq \frac{Rv_A}{v_A + v_{\text{push}}}, \quad \tau \simeq \frac{R}{v_A + v_{\text{push}}}, \quad t_K \simeq \frac{R}{v_A + v_{\text{push}}}. \quad (\text{B4})$$

In the limit $v_{\text{push}} \ll v_A$, the pinch wave outruns the drive and the sheet undergoes kinematic thinning for roughly one Alfvén-crossing time of the original width, $t_K \simeq R/v_A$. When $v_{\text{push}} \sim v_A$, drive and pinch forces balance, yielding a transition approximately halfway through the compression, $t_K \simeq R/(2v_A)$. In this Letter we specifically probe these two regimes. If $v_{\text{push}} \gg v_A$, the drive dominates until near-zero thickness, so $t_K \simeq R/v_{\text{push}}$, but the current sheet does not hold together and breaks apart.

Collapse Time to Skin Depth.—We define the collapse time t_{onset} by the condition that the sheet half-width has shrunk from its initial value R down to the plasma skin depth d_{e0} . We obtain $d_{e0} = a_K \exp[-(t_{\text{onset}} - t_K)/\tau]$, and therefore

$$t_{\text{onset}} \simeq \frac{R}{v_A + v_{\text{push}}} \left[1 + \ln \frac{a_K}{d_{e0}} \right]. \quad (\text{B5})$$

Comments.—Using $v_A = c\sqrt{\sigma_{\text{in}}/(1 + \sigma_{\text{in}})}$, we see that increasing the in-plane magnetization leads to a faster exponential collapse. In the high- σ_{in} limit, $v_A \approx c$, so the thinning time scale $\tau \sim R/(c + v_{\text{push}})$; for low σ_{in} , $v_A \approx c\sqrt{\sigma_{\text{in}}}$ yields $a_K \propto R\sqrt{\sigma_{\text{in}}}$ and slower thinning. In the pinch-dominated regime ($v_{\text{push}} \ll v_A$), $t_{\text{onset}} \sim (R/v_A) \ln(R/d_{e0})$; and in the strongly magnetized limit ($\sigma_{\text{in}} \gg 1$), $t_{\text{onset}} \sim R/c$.

C. LINEAR TEARING MODES

During Phase I, the current sheet thins while small-amplitude tearing-mode perturbations in the out-of-plane flux function A_z grow exponentially. Only modes satisfying $k_x, d_{e0} < 1$ are linearly unstable. Figure 8 shows the time evolution of these linear tearing modes. Here, $\sigma_{\text{in}} = 8$, $v_{\text{push}} = 0.02c$, and $R/d_{e0} = 204$.

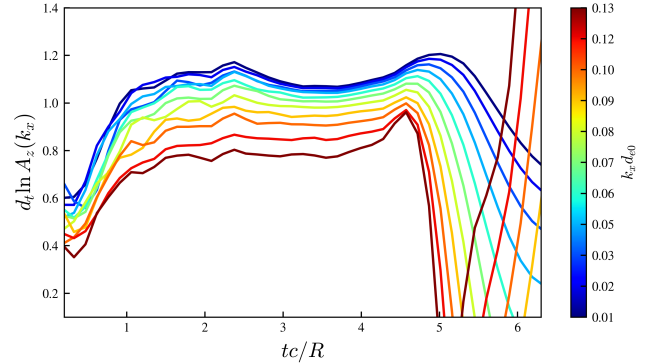


Figure 8. Growth rates of 10 tearing modes computed from a Fourier transform of $A_z(x)$, where A_z is first averaged over y inside the current sheet. The simulation parameters are $\sigma_{\text{in}} = 8$, $v_{\text{push}} = 0.02c$, $R/d_{e0} = 204$

REFERENCES

Abdo, A. A., Ackermann, M., Ajello, M., et al. 2011, *Science*, 331, 739, doi: [10.1126/science.1199705](https://doi.org/10.1126/science.1199705)

Bhattacharjee, A., Huang, Y.-M., Yang, H., & Rogers, B. 2009, *Physics of Plasmas*, 16, 112102, doi: [10.1063/1.3264103](https://doi.org/10.1063/1.3264103)

- Birn, J., Galsgaard, K., Hesse, M., et al. 2005, *Geophys. Res. Lett.*, 32, L06105, doi: [10.1029/2004GL022058](https://doi.org/10.1029/2004GL022058)
- Biskamp, D. 1986, *Physics of Fluids*, 29, 1520, doi: [10.1063/1.865670](https://doi.org/10.1063/1.865670)
- Cerutti, B., Werner, G. R., Uzdensky, D. A., & Begelman, M. C. 2013, *ApJ*, 770, 147, doi: [10.1088/0004-637X/770/2/147](https://doi.org/10.1088/0004-637X/770/2/147)
- Chernoglazov, A., Hakobyan, H., & Philippov, A. 2023, *ApJ*, 959, 122, doi: [10.3847/1538-4357/acffc6](https://doi.org/10.3847/1538-4357/acffc6)
- Comisso, L., & Bhattacharjee, A. 2016, *Journal of Plasma Physics*, 82, 595820601, doi: [10.1017/S002237781600101X](https://doi.org/10.1017/S002237781600101X)
- Comisso, L., Grasso, D., & Waelbroeck, F. L. 2015, *Physics of Plasmas*, 22, 042109, doi: [10.1063/1.4918331](https://doi.org/10.1063/1.4918331)
- Comisso, L., & Jiang, B. 2023, *The Astrophysical Journal*, 959, 137, doi: [10.3847/1538-4357/ad1241](https://doi.org/10.3847/1538-4357/ad1241)
- Comisso, L., Lingam, M., Huang, Y. M., & Bhattacharjee, A. 2016, *Physics of Plasmas*, 23, 100702, doi: [10.1063/1.4964481](https://doi.org/10.1063/1.4964481)
- Comisso, L., & Sironi, L. 2019, *ApJ*, 886, 122, doi: [10.3847/1538-4357/ab4c33](https://doi.org/10.3847/1538-4357/ab4c33)
- Coppi, B., Galvao, R., Pellat, R., Rosenbluth, M., & Rutherford, P. 1976, *Soviet Journal of Plasma Physics*, 2, 533
- Crinquant, B., Cerutti, B., Dubus, G., Parfrey, K., & Philippov, A. 2022, *Phys. Rev. Lett.*, 129, 205101, doi: [10.1103/PhysRevLett.129.205101](https://doi.org/10.1103/PhysRevLett.129.205101)
- Daughton, W., Roytershteyn, V., Karimabadi, H., et al. 2011, *Nature Physics*, 7, 539, doi: [10.1038/nphys1965](https://doi.org/10.1038/nphys1965)
- Del Sarto, D., Pucci, F., Tenerani, A., & Velli, M. 2016, *Journal of Geophysical Research: Space Physics*, 121, 1857, doi: <https://doi.org/10.1002/2015JA021975>
- El Mellah, I., Cerutti, B., & Crinquant, B. 2023, *A&A*, 677, A67, doi: [10.1051/0004-6361/202346781](https://doi.org/10.1051/0004-6361/202346781)
- Furth, H. P., Killeen, J., & Rosenbluth, M. N. 1963, *The Physics of Fluids*, 6, 459, doi: [10.1063/1.1706761](https://doi.org/10.1063/1.1706761)
- Galishnikova, A., Philippov, A., Quataert, E., et al. 2023, *Phys. Rev. Lett.*, 130, 115201, doi: [10.1103/PhysRevLett.130.115201](https://doi.org/10.1103/PhysRevLett.130.115201)
- Goodbred, M., & Liu, Y.-H. 2022, *Phys. Rev. Lett.*, 129, 265101, doi: [10.1103/PhysRevLett.129.265101](https://doi.org/10.1103/PhysRevLett.129.265101)
- Granier, C., Borgogno, D., Comisso, L., et al. 2022, *Phys. Rev. E*, 106, L043201, doi: [10.1103/PhysRevE.106.L043201](https://doi.org/10.1103/PhysRevE.106.L043201)
- GRAVITY Collaboration, Abuter, R., Amorim, A., et al. 2021, *A&A*, 654, A22, doi: [10.1051/0004-6361/202140981](https://doi.org/10.1051/0004-6361/202140981)
- Guo, F., Li, H., Daughton, W., & Liu, Y.-H. 2014, *PhRvL*, 113, 155005, doi: [10.1103/PhysRevLett.113.155005](https://doi.org/10.1103/PhysRevLett.113.155005)
- Hahm, T. S., & Kulsrud, R. M. 1985, *Physics of Fluids*, 28, 2412, doi: [10.1063/1.865247](https://doi.org/10.1063/1.865247)
- Hakobyan, H., Philippov, A., & Spitkovsky, A. 2023a, *The Astrophysical Journal*, 943, 105, doi: [10.3847/1538-4357/acab05](https://doi.org/10.3847/1538-4357/acab05)
- Hakobyan, H., Ripperda, B., & Philippov, A. A. 2023b, *ApJL*, 943, L29, doi: [10.3847/2041-8213/acb264](https://doi.org/10.3847/2041-8213/acb264)
- Hakobyan, H., Spitkovsky, A., Chernoglazov, A., et al. 2023c, *Zenodo*, doi: [10.5281/zenodo.7566725](https://doi.org/10.5281/zenodo.7566725)
- Huang, Y.-M., & Bhattacharjee, A. 2010, *Physics of Plasmas*, 17, 062104, doi: [10.1063/1.3420208](https://doi.org/10.1063/1.3420208)
- Huang, Y.-M., Comisso, L., & Bhattacharjee, A. 2017, *The Astrophysical Journal*, 849, 75, doi: [10.3847/1538-4357/aa906d](https://doi.org/10.3847/1538-4357/aa906d)
- Ji, H., & Daughton, W. 2011, *Physics of Plasmas*, 18, 111207, doi: [10.1063/1.3647505](https://doi.org/10.1063/1.3647505)
- Keppens, R., Porth, O., & Xia, C. 2014, *The Astrophysical Journal*, 795, 77, doi: [10.1088/0004-637X/795/1/77](https://doi.org/10.1088/0004-637X/795/1/77)
- Koide, S., Kudoh, T., & Shibata, K. 2006, *Phys. Rev. D*, 74, 044005, doi: [10.1103/PhysRevD.74.044005](https://doi.org/10.1103/PhysRevD.74.044005)
- Krawczynski, H., Hughes, S. B., Horan, D., et al. 2004, *ApJ*, 601, 151, doi: [10.1086/380393](https://doi.org/10.1086/380393)
- Loureiro, N. F., & Boldyrev, S. 2018, *ApJL*, 866, L14, doi: [10.3847/2041-8213/aae483](https://doi.org/10.3847/2041-8213/aae483)
- Loureiro, N. F., Schekochihin, A. A., & Cowley, S. C. 2007, *Physics of Plasmas*, 14, 100703, doi: [10.1063/1.2783986](https://doi.org/10.1063/1.2783986)
- Lyutikov, M., Pariev, V. I., & Blandford, R. D. 2003, *The Astrophysical Journal*, 597, 998, doi: [10.1086/378497](https://doi.org/10.1086/378497)
- Lyutikov, M., Sironi, L., Komissarov, S. S., & Porth, O. 2017, *Journal of Plasma Physics*, 83, 635830602, doi: [10.1017/S002237781700071X](https://doi.org/10.1017/S002237781700071X)
- Mahlmann, J. F., Levinson, A., & Aloy, M. A. 2020, *MNRAS*, 494, 4203, doi: [10.1093/mnras/staa943](https://doi.org/10.1093/mnras/staa943)
- Mahlmann, J. F., Philippov, A. A., Mewes, V., et al. 2023, *The Astrophysical Journal Letters*, 947, L34, doi: [10.3847/2041-8213/accada](https://doi.org/10.3847/2041-8213/accada)
- Mallet, A. 2020, *Journal of Plasma Physics*, 86, 905860301, doi: [10.1017/S0022377819000941](https://doi.org/10.1017/S0022377819000941)
- Mehlhoff, J., Werner, G., Cerutti, B., Uzdensky, D., & Begelman, M. 2024, *MNRAS*, 527, 11587, doi: [10.1093/mnras/stad3863](https://doi.org/10.1093/mnras/stad3863)
- Mereghetti, S., Rigoselli, M., Salvaterra, R., et al. 2024, *Nature*, 629, 58, doi: [10.1038/s41586-024-07285-4](https://doi.org/10.1038/s41586-024-07285-4)
- Parfrey, K., Beloborodov, A. M., & Hui, L. 2013, *ApJ*, 774, 92, doi: [10.1088/0004-637X/774/2/92](https://doi.org/10.1088/0004-637X/774/2/92)
- Parfrey, K., Giannios, D., & Beloborodov, A. M. 2014, *Monthly Notices of the Royal Astronomical Society: Letters*, 446, L61, doi: [10.1093/mnrasl/slu162](https://doi.org/10.1093/mnrasl/slu162)
- Parfrey, K., Philippov, A., & Cerutti, B. 2019, *Phys. Rev. Lett.*, 122, 035101, doi: [10.1103/PhysRevLett.122.035101](https://doi.org/10.1103/PhysRevLett.122.035101)

- Parker, E. N. 1957, *Journal of Geophysical Research* (1896-1977), 62, 509, doi: <https://doi.org/10.1029/JZ062i004p00509>
- Petropoulou, M., Christie, I. M., Sironi, L., & Giannios, D. 2018, *Monthly Notices of the Royal Astronomical Society*, 475, 3797, doi: [10.1093/mnras/sty033](https://doi.org/10.1093/mnras/sty033)
- Porcelli, F. 1991, *Phys. Rev. Lett.*, 66, 425, doi: [10.1103/PhysRevLett.66.425](https://doi.org/10.1103/PhysRevLett.66.425)
- Pucci, F., Velli, M., & Tenerani, A. 2017, *The Astrophysical Journal*, 845, 25, doi: [10.3847/1538-4357/aa7b82](https://doi.org/10.3847/1538-4357/aa7b82)
- Ripperda, B., Bacchini, F., & Philippov, A. A. 2020, *ApJ*, 900, 100, doi: [10.3847/1538-4357/ababab](https://doi.org/10.3847/1538-4357/ababab)
- Ripperda, B., Liska, M., Chatterjee, K., et al. 2022, *ApJL*, 924, L32, doi: [10.3847/2041-8213/ac46a1](https://doi.org/10.3847/2041-8213/ac46a1)
- Ripperda, B., Porth, O., Sironi, L., & Keppens, R. 2019, *Monthly Notices of the Royal Astronomical Society*, 485, 299, doi: [10.1093/mnras/stz387](https://doi.org/10.1093/mnras/stz387)
- Ripperda, B., Porth, O., Xia, C., & Keppens, R. 2017a, *MNRAS*, 467, 3279, doi: [10.1093/mnras/stx379](https://doi.org/10.1093/mnras/stx379)
- Ripperda, B., Porth, O., Xia, C., & Keppens, R. 2017b, *MNRAS*, 471, 3465, doi: [10.1093/mnras/stx1875](https://doi.org/10.1093/mnras/stx1875)
- Schep, T. J., Pegoraro, F., & Kuvshinov, B. N. 1994, *Phys. Plasmas*, 1, 2843
- Shi, C., Tenerani, A., Velli, M., & Lu, S. 2019, *The Astrophysical Journal*, 883, 172, doi: [10.3847/1538-4357/ab33ff](https://doi.org/10.3847/1538-4357/ab33ff)
- Shibata, K., & Tanuma, S. 2001, *Earth, Planets and Space*, 53, 473, doi: [10.1186/BF03353258](https://doi.org/10.1186/BF03353258)
- Sironi, L., & Spitkovsky, A. 2014, *ApJL*, 783, L21, doi: [10.1088/2041-8205/783/1/L21](https://doi.org/10.1088/2041-8205/783/1/L21)
- Sironi, L., Uzdensky, D. A., & Giannios, D. 2025, *ARA&A*, 63, doi: [10.1146/annurev-astro-020325-115713](https://doi.org/10.1146/annurev-astro-020325-115713)
- Thompson, C. 1994, *Monthly Notices of the Royal Astronomical Society*, 270, 480, doi: [10.1093/mnras/270.3.480](https://doi.org/10.1093/mnras/270.3.480)
- Uzdensky, D. A., Cerutti, B., & Begelman, M. C. 2011, *The Astrophysical Journal Letters*, 737, L40, doi: [10.1088/2041-8205/737/2/L40](https://doi.org/10.1088/2041-8205/737/2/L40)
- Uzdensky, D. A., & Goodman, J. 2008, *The Astrophysical Journal*, 682, 608, doi: [10.1086/588812](https://doi.org/10.1086/588812)
- Uzdensky, D. A., & Kulsrud, R. M. 2000, *Physics of Plasmas*, 7, 4018, doi: [10.1063/1.1308081](https://doi.org/10.1063/1.1308081)
- Uzdensky, D. A., & Loureiro, N. F. 2016, *PhRvL*, 116, 105003, doi: [10.1103/PhysRevLett.116.105003](https://doi.org/10.1103/PhysRevLett.116.105003)
- Werner, G. R., Uzdensky, D. A., Cerutti, B., Nalewajko, K., & Begelman, M. C. 2016, *ApJL*, 816, L8, doi: [10.3847/2041-8205/816/1/L8](https://doi.org/10.3847/2041-8205/816/1/L8)
- Yuan, F., Lin, J., Wu, K., & Ho, L. C. 2009, *Monthly Notices of the Royal Astronomical Society*, 395, 2183, doi: [10.1111/j.1365-2966.2009.14673.x](https://doi.org/10.1111/j.1365-2966.2009.14673.x)
- Yuan, Y., Nalewajko, K., Zrake, J., East, W. E., & Blandford, R. D. 2016, *ApJ*, 828, 92, doi: [10.3847/0004-637X/828/2/92](https://doi.org/10.3847/0004-637X/828/2/92)
- Yuan, Y., Spitkovsky, A., Blandford, R. D., & Wilkins, D. R. 2019, *MNRAS*, 487, 4114, doi: [10.1093/mnras/stz1599](https://doi.org/10.1093/mnras/stz1599)
- Zelenyi, L. M., & Krasnoselskikh, V. V. 1979, *Soviet Ast.*, 23, 460
- Zhang, H., Li, X., Giannios, D., et al. 2020, *ApJ*, 901, 149, doi: [10.3847/1538-4357/abb1b0](https://doi.org/10.3847/1538-4357/abb1b0)